ACS APPLIED MATERIALS & INTERFACES

Research Article

www.acsami.org

Interfacial Thermal Conductance of a Silicene/Graphene Bilayer Heterostructure and the Effect of Hydrogenation

Bo Liu,[†] Julia A. Baimova,[‡] Chilla D. Reddy,[§] Adrian Wing-Keung Law,[∥] Sergey V. Dmitriev,[‡,⊥] Hong Wu,[#] and Kun Zhou*[,†]

[†]School of Mechanical and Aerospace Engineering and [∥]DHI-NTU Center, Nanyang Environmental and Water Research Institute, School of Civil and Environmental Engineering, Nanyang Technological University, 50 Nanyang Avenue, Singapore 639798, Singapore

[‡]Institute for Metals Superplasticity Problems, Russian Academy of Sciences, Ufa 450001, Russia

[§]Institute of High Performance Computing, Singapore 138632, Singapore

[⊥]St. Petersburg State Polytechnical University, Polytechnicheskaya 29, St. Petersburg 195251, Russia

[#]State Key Laboratory of Powder Metallurgy, Central South University, Changsha, Hunan 410083, People's Republic of China

ABSTRACT: van der Waals heterostructures, obtained by stacking layers of isolated two-dimensional atomic crystals like graphene (GE) and silicene (SE), are one of emerging nanomaterials for the development of future multifunctional devices. Thermal transport behaviors at the interface of these heterostructures play a pivotal role in determining their thermal properties and functional performance. Using molecular dynamics simulations, the interfacial thermal conductance G of an SE/GE bilayer heterostructure is studied. Simulations show that G of a pristine SE/GE bilayer at room temperature is 11.74 MW/m^{2}K when heat transfers from GE to SE, and is 9.52 MW/m^{2}K for a reverse heat transfer, showing apparent thermal rectification effects. In addition, G increases monotonically with both the temperature and the interface coupling strength. Furthermore, hydrogenation of GE is efficient in enhancing G if an optimum hydrogenation pattern is adopted. By changing the hydrogen coverage f, G can be controllably manipulated and maximized up to five times larger than that of pristine SE/GE. This study is helpful for understanding the interface thermal transport behaviors of novel van der Waals heterostructures and provides guidance for the design and control of their thermal properties.

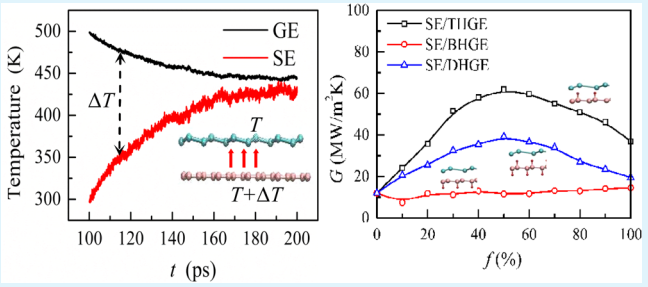

KEYWORDS: *graphene, silicene, van der Waals heterostructure, interface thermal conductance, hydrogenation, molecular dynamics simulation*

1. INTRODUCTION

Graphene (GE), a monolayer graphite, possesses great potential in next-generation nanotechnologies due to its unique electronic,[1] mechanical,[2−6] and thermal properties.[7,8] Interesting physical phenomena such as discrete breathers have also been observed in GE.[9,10] Inspired by successful studies of GE, many efforts have also been devoted to searching new forms of low-dimensional materials. Silicene (SE), consisting of Si atoms, has the same two-dimensional honeycomb lattice structure.[11,12] Similar to GE, SE was found to have a linear dispersion in the vicinity of Dirac points and thus can bring about excellent electronic properties.[13,14]

In GE, C atoms are bonded through pure sp^2 hybridization and lie in a planar plane. In contrast, with a larger ionic radius the Si atoms in SE interact with each other through a mixture of sp^2 and sp^3 hybridizations and are arranged in a low-buckled manner.[11] This buckling makes it possible to tune the band gap of SE through externally applied electric fields, a method that is not applicable to GE.[15] Furthermore, there exists the interplay between the electromagnetic field and spin−orbit coupling in SE, a feature that can be utilized to probe the physics in quantum phase transition. As a result, SE has been proposed as a potential candidate for overcoming the limitation of GE in novel electronic devices.

In parallel with the efforts on searching and studying GE-like materials, another research field has recently emerged and attracted a lot of attentions.[16] It deals with heterostructures and devices constructed by vertically stacking different two-dimensional crystals on top of each other. The resulting stack represents an artificial material assembled in a chosen sequence with blocks defined with one-atomic-plane precision. Between different stack layers, atoms interact with each other via weak van der Waals forces. By designing the stacking sequence, heterostructures with fascinating properties can be achieved. So

Received: August 4, 2014
Accepted: October 2, 2014
Published: October 13, 2014

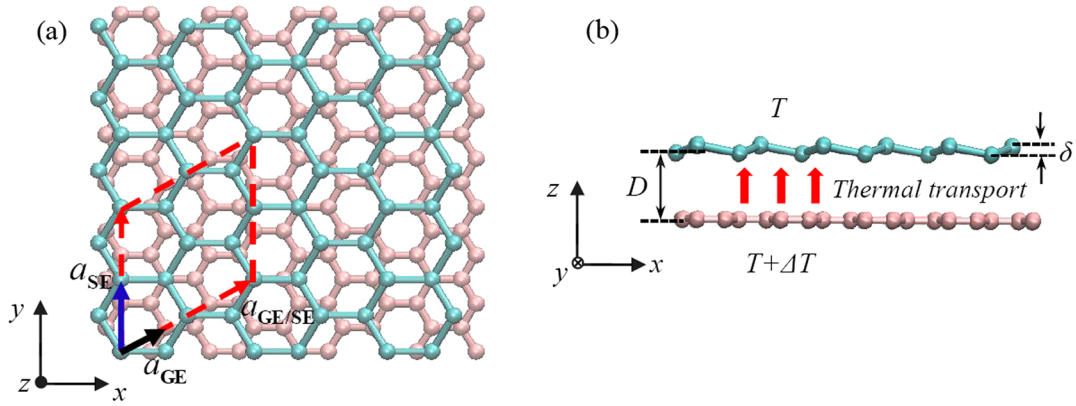

Figure 1. Atomic structure of the SE/GE heterostructure: (a) top and (b) side views. The pink and green balls represent the C and Si atoms, respectively.

far, several kinds of such van der Waals heterostructures have been successfully synthesized and are found to work exceptionally well in practice.[17−19]

In terms of heterostructures composed by GE and SE, recent first-principles calculations have demonstrated that a free-standing SE sheet on a single GE sheet or between two GE sheets can be stabilized at room temperature.[20−24] Because of the weak van der Waals interaction between SE and GE, the excellent electronic properties of both GE and SE are preserved.[23] Furthermore, novel electronic and optical properties can be induced in the SE/GE heterostructures.[24]

So far, the thermal transport behaviors of the SE/GE heterostructure, particularly the thermal conductance across the interface between SE and GE remains unknown. At the nanoscale, the nanoelectronics face severe challenges from Joule heating induced by electronic current, which leads to high power density and spatial localization of heat.[25] Such localized heat, if not dissipated efficiently, would nucleate thermal hot spots, limit the maximum electronic current density, and potentially cause materials failure. Previous studies have indicated that the thermal conductivity of SE is low and in the range of 3−40 W/mK.[26−30] The low thermal conductivity of SE made the heat dissipation challenge in the SE/GE heterostructure more severe.

Previous studies have shown that the low thermal conductance at the interface of low-dimensional materials such as GE and carbon nanotubes (CNTs) with their substrates or surrounding matrixes is a major limitation for effective thermal transport and heat dissipation.[31−33] For example, because of the low thermal conductance at the CNT/polymer interface, polymer-based composites with CNTs as reinforcing phases show only a modest increase in thermal conductivity over that of pure polymer matrices,[34] despite CNT being an excellent thermal conductor.

To enhance the interfacial thermal conductance, surface engineering approaches including chemical functionalization[35,36] and atomic intercalation[37] are usually adopted. As one important chemical functionalization method, hydrogenation is often adopted to tune the mechanical and physical properties of GE.[38−40] Moreover, hydrogenation of GE is reversible and can be applied controllably in different patterns.[41]

Hence, this work aims to study the thermal conductance at the interface of a SE/GE bilayer heterostructure via molecular dynamics (MD) simulations. The effects of temperature, interface coupling strength, thermal transport direction and hydrogenation of GE are investigated and understood by the phonon spectra analyses. Different GE hydrogenation patterns and coverages are concerned.

2. MODELING

The lattice constants for GE and SE are a_{GE} = 2.46 Å and a_{SE} = 3.89 Å, respectively. To model the SE/GE bilayer heterostructure, we deposited the SE layer on the GE layer, as illustrated in Figure 1. The supercell of the SE/GE heterostructure consists of a 2 × 2 supercell of SE and a 3 × 3 supercell of GE, and is delineated by the red dotted line. Accordingly, the lattice constant of the heterostructure is taken as $a_{GE/SE} = (3a_{GE} + 2a_{SE})/2$ = 7.58 Å, with a small lattice mismatch of ∼2.5% for both GE and SE. This lattice mismatch is close to that from the recent first-principles calculations of one SE layer sandwiched between two GE layers.[22] A comparable lattice mismatch of ∼1.9% has also been observed in a similar system (hybrid GE/MoS_2 bilayer).[42] Reportedly, the packing patterns of GE and SE, which describe the relative in-plane position between them, have a negligible effect on the structural stability and physical properties of the SE/GE heterostructure.[24] Therefore, the packing pattern effect is not taken into account in this work.

To capture the buckling feature of SE, the Si atoms in SE are initially displaced in an out-of-plane mode with the buckling distance δ = 0.42 Å (Figure 1b). The interlayer distance D, defined as the average vertical Si−C distance along the out-of-plane z direction, is set to be 3.60 Å, according to previous first-principles calculations.[23,24] The in-plane dimensions of the heterostructure are set as 10.5 nm × 10 nm.

The simulations are conducted by using the large-scale atomic/molecular massively parallel simulator (LAMMPS) package.[43] Periodic boundary conditions are applied along the in-plane x and y directions to remove the edge effect, with the free boundary condition along the out-of-plane direction. To model the interactions of C−C atoms and those of C−H atoms, the adaptive intermolecular reactive empirical bond order (AIREBO) potential derived from the second-generation Brenner potential is adopted.[44] The Stinllinger−Weber (SW) potential[45] with a recently developed parameter set[28] is used to describe the interactions of the Si−Si atoms. The earlier works by the present authors demonstrated that the SW potential can provide a good description of the atomic configuration of SE by preserving its initial out-of-plane buckling.[30,46]

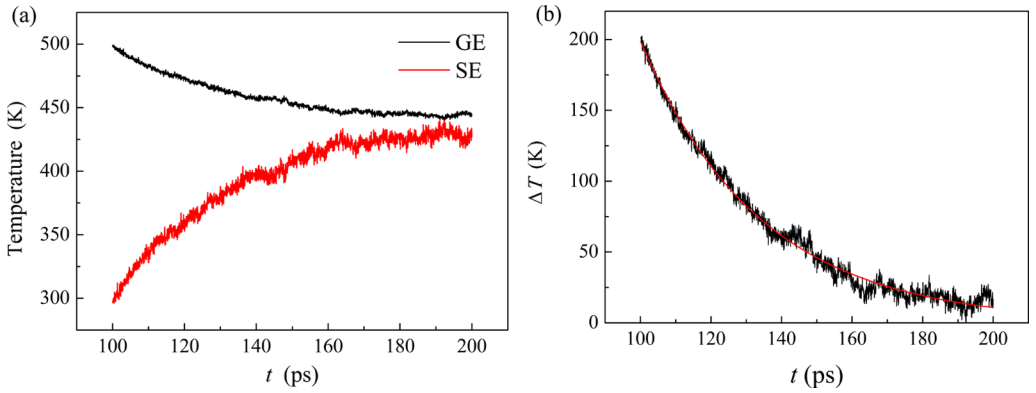

Figure 2. (a) Evolution of the temperatures of SE and GE, and (b) their difference ΔT during the thermal relaxation. The exponential fitting in b is performed to obtain the relaxation time τ.

To model the weak van der Waals force between SE and GE, the 12−6 Lennard−Jones (LJ) potential is adopted as follows:

$$V(r) = 4\chi\varepsilon\left[\left(\frac{\sigma}{r}\right)^{12} - \left(\frac{\sigma}{r}\right)^{6}\right] \quad (1)$$

Here, r represents the distance of two atoms, ε is the energy that reflects their interaction strength, σ denotes the zero-across distance of the potential, and χ is a scaling factor and can be used to tune the interaction strength. These parameters are given as ε_{Si-C} = 8.909 meV,σ_{Si-C} = 3.326 Å, ε_{Si-H} = 5.767 meV, and σ_{Si-H} = 2.932 Å, according to the universal force field developed by Rappe et al.[47] The cutoff distance of the LJ potential is set to be 10 Å, a value that is about three times σ_{Si-C} = 3.326 Å.

The thermal relaxation simulations, which mimic the experimental pump−probe approach, are performed to calculate the interfacial thermal conductance G. At first, the initial configuration of the SE/GE bilayer is equilibrated at T = 300 K under the constant volume and temperature ensemble (NVT) for 50 ps with a time step of 0.1 fs. Upon realization of the equilibrium state, a temperature difference ΔT between GE and SE is then constructed by rapidly increasing GE to $T+\Delta T$ through the velocity rescaling method, while keeping SE at T (Figure 1b). To stabilize ΔT, we conducted the simulation for another 50 ps during which GE and SE are placed in two separate thermostats to remain at $T+\Delta T$ and T, respectively.

Afterward, the system is switched to the constant volume and energy ensemble (NVE) with the thermostats removed. In the absence of temperature control, the system is allowed to relax thermally and the temperature difference ΔT decays with the time t in an exponential manner as $\Delta T(t) = \Delta T(t_0)\exp[(t_0 - t)/\tau]$, where t_0 is the starting time of the thermal relaxation process and τ is the thermal relaxation time to be determined. In the simulation, ΔT = 200 K was found to be a proper temperature difference. If ΔT is too small, the thermal relaxation process will be very noisy, making it difficult to apply the lumped heat-capacity model and calculate the thermal relaxation time τ. On the other hand, if ΔT is too large, it will become difficult to determine the temperature dependence of the interfacial thermal conductance G. The same temperature difference of ΔT= 200 K was adopted previously to study the interface thermal conductance between CNT and its surrounding matrix.[33,48]

Given that the thermal conductance G of the interface is much smaller than that of GE, it can be calculated based on the lumped heat-capacity model as[33]

$$G = C_V/(A\tau) \quad (2)$$

Here, A is the interface area, and C_V is the effective constant volume heat capacity of the SE/GE bilayer system, which can be calculated by $C_V = C_{GE}C_{SE}/(C_{GE}+C_{SE})$ according to the previous study.[48] Here, C_{GE} and C_{SE} are the constant volume heat capacity of the GE and SE layers, respectively, and can be obtained by

$$C = 3Nk_B\int_0^\infty P(\omega)\left(\frac{h\omega}{k_BT}\right)^2\exp\left(\frac{h\omega}{k_BT}\right) \Big/ \left(\exp\left(\frac{h\omega}{k_BT}\right) - 1\right)^2 d\omega \quad (3)$$

In eq 3, N denotes the number of atoms, k_B is the Boltzmann constant, h is the Planck constant, T is the temperature, and $P(\omega)$ is the phonon spectrum power at the frequency ω which can be calculated by performing the fast Fourier transform on the velocity autocorrelation function as[30]

$$P(\omega) = \frac{1}{\sqrt{2\pi}}\int_0^\infty e^{i\omega t}\langle\sum_{j=1}^{N} v_j(t)v_j(0)\rangle d\omega \quad (4)$$

where $v_j(t)$ denotes the velocity of the atom j at time t. The ensemble average in eq 4 is realized by time averaging over a period of 50 ps with the sample velocities extracted from the simulation every 5 fs.

Equation 3 shows that the heat capacity C_{GE} or C_{SE} is a function of temperature T. More specifically, both C_{GE} and C_{SE} increase with T because more phonon modes will be excited in GE and SE at higher temperatures. As a result, C_{GE} decreases and C_{SE} increases during the thermal relaxation process because the temperature of GE layer decreases, whereas that of the SE layer increases. Calculations show that after the thermal relaxation, C_{GE} decreases by no more than 7%, whereas C_{SE} increases by no more than 2%. To apply the lumped heat-capacity model, which assumes constant C_V, we neglected the changes of C_{GE} and C_{SE} during the thermal relaxation. Most of the previous studies regarded C_V as a constant and used it for calculating G at different temperatures.[33,48] The present study takes into account the temperature dependence of C_V. The G of the SE/GE bilayer for a given temperature T is calculated by

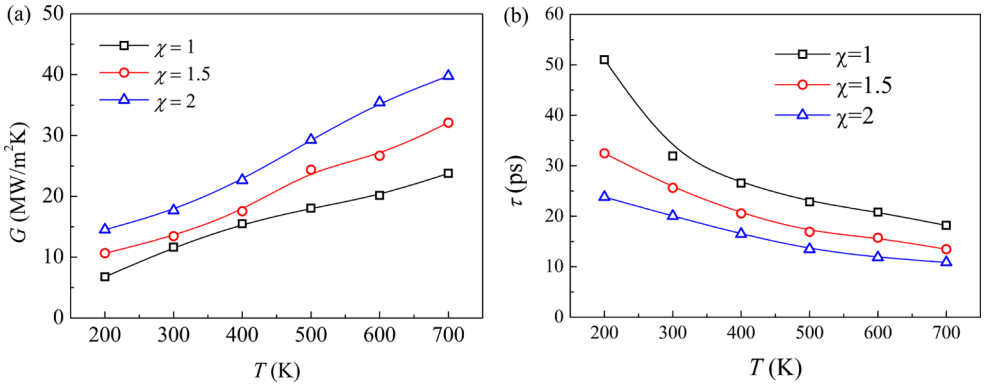

Figure 3. Dependence of (a) the interfacial thermal conductance G and (b) thermal relaxation time τ on the temperature T for different values of χ.

utilizing the value of C_V obtained at the final equilibrium temperature of the bilayer (this temperature is somewhere between T and $T+\Delta T$).

3. RESULTS AND DISCUSSIONS

3.1. Interfacial Thermal Conductance G. Figure 2a shows the temperature evolutions for both GE and SE during the thermal relaxation at T = 300 K. As time passes, the temperature of GE decreases, whereas that of SE increases, indicating heat transfer from GE to SE. Since GE and SE have different heat capacities per area, their bilayer does not equilibrate at their middle temperature of 400 K. The final equilibrium temperature of the SE/GE bilayer is closer to the initial temperature of GE than that of SE because GE has a larger heat capacity per area than SE. The simulation shows that when GE and SE are set at 500 and 300 K, respectively, their bilayer eventually equilibrates at ~440 K. In contrast, if GE and SE are set at 300 and 500 K, respectively, the system reaches the equilibrium temperature of ~360 K.

As shown in Figure 2b, the temperature difference ΔT between GE and SE exponentially decays, which agrees well with the theoretical model. Exponential fitting of the curve gives the relaxation time τ as 31.95 ps. Therefore, the dependence of ΔT on t is obtained to be $\Delta T(t) = \Delta T(t_0)\exp[(t_0 - t)/31.95]$. Using eqs 2−4, the interfacial thermal conductance G of the SE/GE heterostructure at 300 K is calculated to be 11.74 MW/m^{2}K. Simulations have also been conducted for ΔT = 100 K and ΔT = 150 K. The simulation results show that large fluctuation occurs to the $\Delta T(t)$ curve when ΔT = 100 K and the fluctuation reduces when ΔT increases to 150 K. For ΔT = 150 K, G is calculated as 11.28 MW/m^{2}K, which is close to that obtained for ΔT = 200 K. The obtained G is on the same order of those found for several other GE-based interfaces, e.g., 21 MW/m^{2}K for the GE/resin interface[49] and 28 MW/m^{2}K for the GE/Si interface.[50]

3.2. Effect of Temperature and Interface Coupling Strength. Nanoelectronic devices usually work at high temperatures because of the existence of hot spots and their high heat densities. The dependence of the interfacial thermal conductance G on the temperature T is investigated for various scaling factors χ. The temperature difference is kept at ΔT = 200 K. Simulations show that the interlayer distance D almost does not change with χ. Figure 3a indicates that G increases monotonically with both T and χ. As T increases from 200 to 700 K, G is increased by three to four times. This temperature dependence of G is in good consistence with those found at the interfaces of GE/Cu[51] and CNT/SiO$_2$.[33]

According to eq 2, the interfacial thermal conductance G depends on the effective heat capacity C_V and the thermal relaxation time τ for a given interface area A. Figure 3b shows that τdecreases monotonically with T. As T increases from 200 to 700 K, the τ for χ = 1is reduced by 65% (which means 186% increase for G) and the C_V increases by 25%. This means the change in the initial temperature T of the SE/GE heterostructure affects the interfacial thermal conductance mainly through changing the thermal relaxation time τ.

The dependence of the thermal relaxation time τ on the temperature T can be explained by analyzing the phonon spectra of GE and SE, as shown in Figure 4. Because GE is

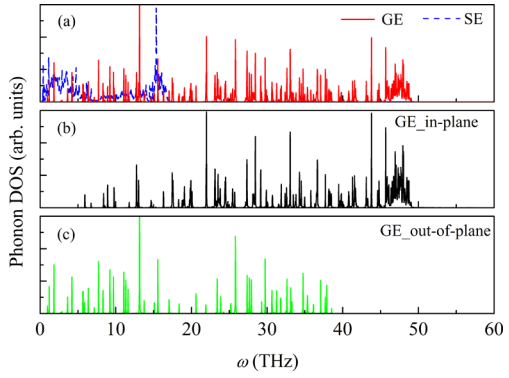

Figure 4. (a) Total phonon spectra of GE and SE, and the decomposition of the GE spectrum into (b) in-plane and (c) out-of-plane components.

highly anisotropic, its spectrum is further decomposed into in-plane and out-of-plane components. It is observed that most of the overlaps between the phonon spectra of GE and SE are located in the low frequency range of 1−17 THz, and the out-of-plane component of the GE spectrum contributes mostly to these overlaps. This implies that the coupling between the phonons in SE and the low-frequency out-of-plane phonons in GE provides the main channel for thermal transport across the SE/GE interface. This is in good agreement with the observations from the interfaces between GE and other materials such as polymer.[52]

At low temperature T, fewer phonons are excited in GE. As a consequence, the coupling between the phonons across the interface is reduced, which limits the thermal transport and leads to a larger relaxation time τ and thus a smaller interfacial thermal conductance G. As T increases, more phonons, especially those with high frequencies, are excited in GE.

Moreover, the Umklapp phonon scattering process is enhanced with increasing temperature. As a result, these high-frequency phonons can be scattered into multiple low-frequency ones, which can then be coupled with the phonons in SE and contribute to the interface thermal transport, thus resulting in the increase of G.

The increase in the interfacial thermal conductance G with the interface coupling strength χ can be explained from two aspects: (1) the coupling between the phonons of GE and SE is enhanced, which directly increases the efficiency of the interfacial thermal transport; (2) the coupling between the in-plane and out-of-plane phonons in GE is strengthened, which indirectly facilitates the heat transfer from GE to SE, as explained as follows.

In free-standing GE, the in-plane and out-of-plane phonons are well decoupled.[53] Most of the in-plane phonons have frequencies beyond the overlap range of 1−17 THz (Figure 4) and cannot contribute to the heat transport. When SE is located on GE, its various symmetries (e.g., reflection, translation, and rotation) are broken, and the vibrations of its C atoms are altered by the GE-SE interactions, especially at the sites where the C and Si atoms share the same in-plane coordinates. As a result, the C atoms at these sites serve as scattering centers for the in-plane phonons of GE, which leads to the coupling of in-plane and out-of-plane phonons. Part of the heat stored in the in-plane phonons of GE can be transferred to the out-of-plane ones and then transmitted to SE. This increases the heat transfer between GE and SE and thus the interfacial thermal conductance.

3.3. Effect of Thermal Transport Directions. Nanoscale systems with structure asymmetry and lattice anharmonicity can be utilized as thermal rectifiers which are one kind of the most fundamental thermal devices to be realized experimentally.[54−56] In a thermal rectifier, the heat transport depends on the direction and the thermal conductance is larger in one direction than in the reserve direction. To investigate the effect of thermal transport direction on the interfacial thermal conductance G of the SE/GE bilayer, the transport direction in Figure 1b is reversed by setting the temperature of SE at $T+\Delta T$ and that of GE at T. Because of the different atom densities per area for GE and SE, they equilibrate at a different temperature to that when heat transfers from GE to SE. For example, at 300 K, the SE and GE layers equilibrate at ∼360 K instead of 440 K when heat transfers from SE to GE.

Figure 5 shows the interfacial thermal conductance G with the thermal transport from SE to GE (denoted as $G_{S\to G}$) and that with the thermal transport in the reverse direction (denoted as$G_{G\to S}$) at different temperatures T. It is found that $G_{S\to G}$ is much smaller than $G_{G\to S}$ at any given temperature. Thermal rectification ratio is defined as $\eta = (G_{G\to S}-G_{S\to G})/G_{S\to G}$. At T = 300 K, $G_{S\to G}$ equals 9.52 MW/m^{2}K, which is only ∼80% of $G_{G\to S}$, leading to $\eta \approx 0.23$. This rectification ratio is comparable to those found in several GE-based nanostructures, such as the GE nanoribbons with asymmetric isotope doping.[56]

The thermal rectification in the SE/GE bilayer is mainly because of two reasons: (1) different temperature dependences of SE and GE for the heat capacity and (2) different atom densities per area of SE and GE.

As the temperature T increases, more phonons are excited in both GE and SE. These newly excited phonons not only participate in the interface thermal transport but also lead to increase in the heat capacities of the SE and GE layers. As T increases from 300 to 500 K, the heat capacity C_{GE} of the GE layer increases by ∼20%, whereas the C_{SE} of the SE layer increases only by ∼3.5%. This indicates that more phonons are available for interface coupling in the case where the GE layer is increased to 500 K with SE being set at 300 K than the case where SE is increased to 500 K with GE set at 300 K. Although most of the newly excited phonons in GE have high frequencies and do not directly participate in the interface heat transport, they can be scattered into multi low-frequency ones and then coupled with the phonons in SE because of the enhanced Umklapp scattering at high temperatures.

The atom density per area of the GE layer is 2.25 times larger than that of the SE layer. During the temperature increase, the larger atom density per area of the GE layer also brings about more phonon excitation to contribute to the interface thermal transport. Therefore, the interface thermal conductance G is larger when heat transfers from GE to SE than in a reverse transfer direction, leading to the thermal rectification effect.

3.4. Effect of GE Hydrogenation. Chemical functionalization of GE by introducing atoms of different species or atomic groups to modify its physical, chemical and mechanical properties has attracted significant attraction. As one of the chemical functionalization methods, hydrogenation is efficient in tuning the thermal properties of GE.[8,57] Two typical patterns of hydrogenated GE (HGE) have been reported.[38,41,58] One pattern is to obtain graphane, a fully double-sided HGE (DHGE) sheet with hydrogen atoms bonded to carbon atoms on both sides of GE alternatively (Figure 6a). The other one realizes graphone, a single-sided HGE (SHGE) sheet, by utilizing the reversibility of the hydrogenation process, i.e., removing all the hydrogen atoms on one side of DHGE sheet

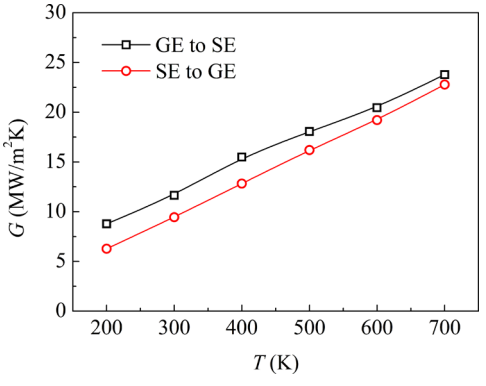

Figure 5. Interface thermal conductance G with the thermal transport from GE to SE and from SE to GE at various temperatures T.

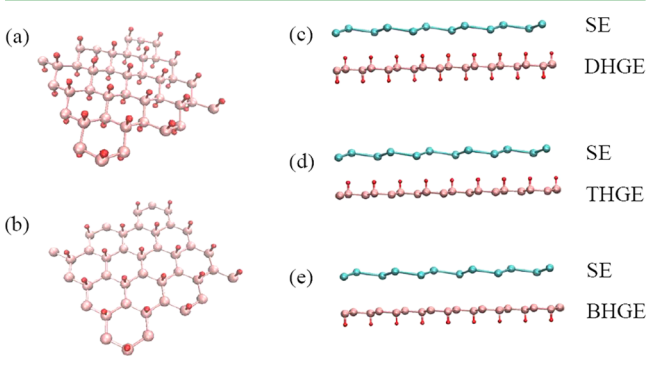

Figure 6. Atomic configurations of (a) DHGE, (b) SHGE, (c) SE/DHGE, (d) SE/THGE, and (e) SE/BHGE.

(Figure 6b). This work utilizes both patterns to construct SE/DHGE and SE/SHGE heterostructures.

Figure 6c shows the atomic configuration of the SE/DHGE heterostructure. In real application, the hydrogen coverage f of the SE/DHGE may not be full. Here, a partial hydrogen coverage is obtained by randomly removing the same number of H atoms on both sides of DHGE; that is to say, a random distribution pattern of the H atoms is considered. Thus, the present study focuses on the coverage ratio of the H atoms rather than the details of their distributions, although the latter might also affect the interfacial thermal conductance. The hydrogen coverage is defined as $f=N_1/N_0$, where N_0 denotes half the number of the total C atoms in GE and N_1 denotes the number of the H atoms on one side. To obtain the SHGE with the same hydrogen coverage f, we removed all the hydrogen atoms on one side of the DHGE with the coverage f. As shown in panels d and e in Figure 6, according to the position of the H atoms on GE, the SE/SHGE heterostructure is further classified into two types: SE/THGE (top side) and SE/BHGE (bottom side). It is worth pointing out that after hydrogenation, the interlayer distance D increases slightly with the hydrogen coverage f, especially when the H atoms are located at the SE/GE interface. At f = 100%, D equals 4.12, 4.02, and 3.70 Å for SE/DHGE, SE/THGE, and SE/BHGE, respectively.

Figure 7 shows the dependence of the interfacial thermal conductance $G_{G\to S}$ on the hydrogen coverage f for all the three

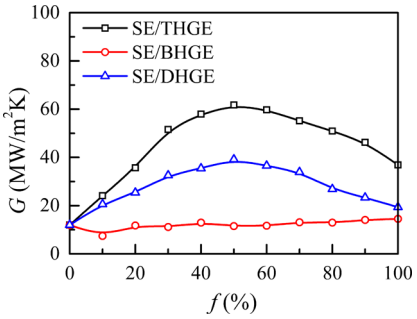

Figure 7. Dependence of interfacial thermal conductance G on the hydrogen coverage f for three types of SE/THGE heterostructures.

types of SE/HGE heterostructures. Since similar trends are found for $G_{S\to G}$, only the results for $G_{G\to S}$ is presented here and the general term G is used in the following discussion for simplicity. It is found that for both SE/THGE and SE/DHGE that have the H atoms at the SE/GE interface, G dramatically increases as f increases up to$f$ = 50% and then decreases.

In contrast, for SE/BHGE that does not have interfacial H atoms, G first decreases and then slightly increases after f > 10%. Overall, the change in G for SE/BHGE is almost negligible as compared to those for both SE/THGE and SE/DHGE. This indicates that hydrogenation is more efficient in tuning G when the H atoms are located between SE and GE. The maximum values of G for SE/THGE and SE/DHGE are 61.75 and 39.14 MW/m^{2}K, respectively, which are three to five times higher than that of the pristine SE/GE heterostructure.

For the SE/HGE heterostructures, thermal transport across the interface occurs through both the interaction of the Si−H atoms and that of the Si−C atoms. To illustrate the contribution of Si−H interaction, the van der Waals interaction of Si−C atoms is turned off by setting $\varepsilon_{Si-H} \neq 0$ and $\varepsilon_{Si-C} = 0$. Alternatively, to illustrate the Si−C interaction, the van der Waals interaction of Si−H atoms is turned off by setting $\varepsilon_{Si-H} = 0$ and $\varepsilon_{Si-C} \neq 0$. For both assumed scenarios, the interfacial thermal conductance G for the SE/THGE with χ = 1 is calculated for various hydrogen coverages f, as shown in Figure 8. For comparison, the results for the scenario that considers full interactions ($\varepsilon_{Si-H} \neq 0$ and $\varepsilon_{Si-C} \neq 0$) are presented as well.

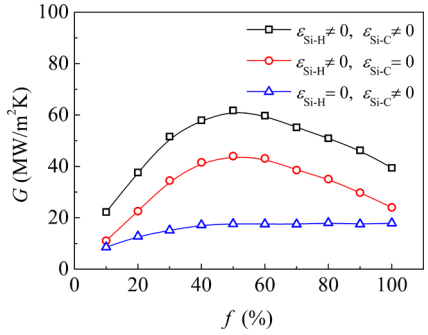

Figure 8. Interfacial thermal conductance G of SE/THGE versus its hydrogen coverage f for different atomic interaction conditions.

When $\varepsilon_{Si-H} \neq 0$ and ε_{Si-C} = 0, G increases with f until $f \approx$ 50%and then decreases afterward. This nonmonotonic dependence is related to two mechanisms. On the one hand, as f increases, more H atoms participate to interact with Si atoms and thus enhance the interface thermal transport. On the other hand, H atoms have a small atomic mass and tend to vibrate at high frequencies.

Figure 9 presents the phonon spectra of the H atoms in the low-frequency range for three different hydrogen coverages. It

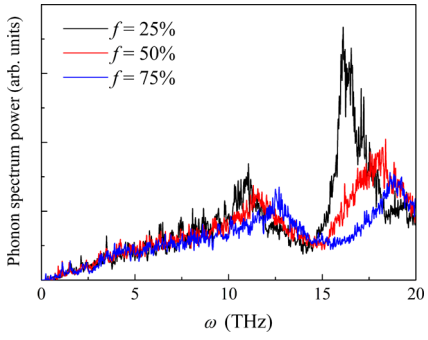

Figure 9. Phonon spectra of H atoms in the low-frequency range for three different hydrogen coverages f.

shows that as f increases, the phonon spectrum shifts toward the high-frequency direction, and the spectrum power also dramatically decreases particularly in the range of 15−20 THz. As a result, the coupling between the phonons of the H atoms and those of the Si atoms is weakened, resulting in the reduction of the interface thermal transport. The two mechanisms compete to determine the interfacial thermal conductance G. When f is small, the former mechanism is dominant; when f is large, the latter one becomes dominant, thus resulting in a nonmonotonic dependence of G on f.

When ε_{Si-H} = 0 and $\varepsilon_{Si-C} \neq 0$, G increases with f upon $f \approx$ 50%and then stabilizes. This increase of G is due to the enhanced coupling between the in-plane and out-of-plane phonons of C atoms. Figure 10 plots the in-plane and out-of-plane components of the phonon spectra for the C atoms in THGE. It shows that as f increases from 25 to 50%, the overlap

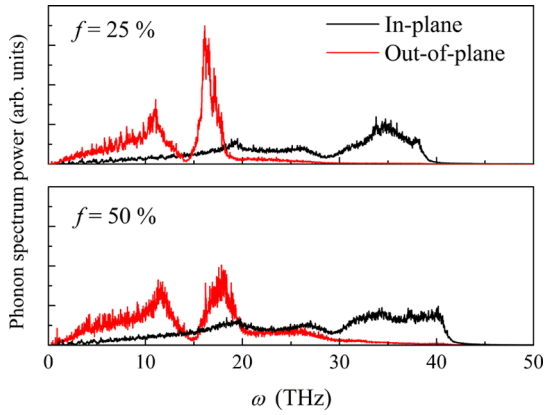

Figure 10. In-plane and out-of-plane components of the phonon spectra for the C atoms in THGE for two different hydrogen coverages.

between the in-plane and out-of-plane spectrum components dramatically increases, particularly in the frequency range of 15−30 THz. This results in an enhanced coupling between the in-plane and out-of-plane phonons, which can facilitate the heat transfer from THGE to SE. When $f > 50\%$, the overlap does not change much, thus leading to that G almost remains the same.

When $\varepsilon_{Si-H} \neq 0$ and $\varepsilon_{Si-C} \neq 0$, the interfacial thermal conductance G of SE/THGE changes with the hydrogen coverage f in the same manner as that for $\varepsilon_{Si-H} \neq 0$ and $\varepsilon_{Si-C} = 0$. A similar phenomenon is observed for SE/DHGE. This indicates that hydrogenation affects G of SE/HGE mainly through the Si−H interaction.

Figure 8 also shows that the interfacial thermal conductance G of SE/THGE with full interactions being taken into account ($\varepsilon_{Si-H} \neq 0$ and $\varepsilon_{Si-C} \neq 0$) is approximately the summation of G with only Si−C interactions ($\varepsilon_{Si-H} = 0$ and $\varepsilon_{Si-C} \neq 0$) and G with only Si−H interactions ($\varepsilon_{Si-H} \neq 0$ and $\varepsilon_{Si-C} = 0$). It implies that the effect of Si−H interactions on the thermal transport across the SE/HGE interface is decoupled with that of the Si−C interactions.

Besides the hydrogen coverage f, the hydrogenation pattern can also significantly affect the interfacial thermal conductance G of SE/HGE. The G of SE/DHGE always lies between those of SE/THGE and SE/BHGE, regardless of f (Figure 7). This effect is caused mainly by the change in the average vertical distance d_{Si-H} for the Si−H atoms along the out-of-plane direction due to different hydrogenation patterns.

When H atoms are bonded to C atoms in GE, the latter ones are pulled away from their initial positions with an out-of-plane displacement of ∼0.25 Å along the Z direction. Such displacement is positive when H atoms are located on the top side of GE, but negative when H atoms are on the bottom side. As a result, for SE/THGE, the Si−H atoms have d_{Si-H} = 4.02−1.10−0.25 = 2.67 Å, which is much smaller than the d_{Si-H} = 3.70 + 1.10 + 0.25 = 5.05 Å for SE/BHGE. With a larger d_{Si-H}, the van der Waals interaction of the Si−H atoms becomes weaker. Considering the fact that the Si−H interaction plays a dominant role in determining the interfacial thermal conductance G of SE/HGE as demonstrated above, the G of SE/THGE is much larger than that of SE/BHGE. In addition, due to the large d_{Si-H} for SE/BHGE, the interaction of the Si−H atoms is very weak and contributes little to the interface thermal transport. As a result, the G of SE/BHGE is almost independent of the hydrogen coverage f (Figure 7).

In SE/DHGE, the H atoms on the top side of GE is much closer to the Si atoms than those on the bottom side, and thus contribute most to the interface thermal transport. These top H atoms have the average Si−H distance of d_{Si-H} = 4.12−1.10−0.25 = 2.77 Å, a value that is slightly larger than the d_{Si-H} = 2.67 for SE/THGE. Moreover, the interlayer distance of D = 4.12 Å for SE/DHGE is also larger than the D = 4.02 Å for SE/THGE. Therefore, both the Si−H and the Si−C interactions are weaker for SE/DHGE, leading to it having a smaller G than SE/THGE.

More importantly, because of double-sided hydrogenation, DHGE has two times larger number of H atoms than THGE for the same hydrogen coverage. As a result, more phonons have high frequencies in DHGE, and the coupling between the phonons of H atoms and those of Si atoms in SE/DHGE becomes weaker than that in SE/THGE, as indicated in Figure 9. This weakening effect is also responsible for the lower G of SE/DHGE than that of SE/THGE.

4. CONCLUSIONS

The interfacial thermal conductance G of a SE/GE heterostructure is studied using molecular dynamics simulations. The effect of temperature, interface coupling strength, thermal transport direction and GE hydrogenation is investigated. The G of pristine SE/GE heterostructure at room temperature is calculated as 11.74 MW/m^{2}K when the heat transfers from GE to SE, and is 9.52 MW/m^{2}K when from SE to GE, showing a high thermal rectification ratio.

Furthermore, it is found that G increases monotonically with both the temperature and the interface coupling strength. As the temperature increases, the Umklapp phonon scattering process in GE is enhanced to produce more low-frequency phonons from high-frequency ones. These low-frequency phonons in GE can then be coupled with the phonons in SE, which contributes to the interface thermal transport and results in the increase of G. As the interface coupling strength increases, not only the coupling between the phonons of GE and SE enhanced, but also the coupling between the in-plane and out-of-plane phonons in GE is strengthened, which both facilitate the heat transfer from GE to SE and thus bring about the increase in G.

Double-sided and single-sided hydrogenation patterns are used to construct the SE/DHGE and SE/SHGE (including SE/THGE with H atoms on the top side of GE and SE/BHGE with H atoms on the bottom side) heterostructures, respectively. It is found that SE/DHGE and SE/THGE have much larger interfacial thermal conductance than pristine SE/GE, and SE/THGE has the largest value. However, hydrogenation has almost no effect on the interfacial thermal conductance of SE/BHGE. Furthermore, it is found that as the hydrogen coverage f increases, G first increases and then decreases for both SE/DHGE and SE/THGE, but remains almost unchanged for SE/BHGE. At $f \approx 50\%$, a maximum G of 61.75 MW/m^{2}K is obtained for SE/THGE, which is about five times larger than that of pristine SE/GE. These phenomena are well explained by the interactions of the Si−H atoms and those of the Si−C atoms.

This study is helpful for understanding the thermal transport behaviors of SE/GE heterostructures and other multilayered two-dimensional nanomaterials, which can contribute to promoting their potential applications.

AUTHOR INFORMATION

Corresponding Author

*E-mail: kzhou@ntu.edu.sg. Tel.: +65 6790 5499. Fax: +65 6792 4062.

Notes

The authors declare no competing financial interest.

ACKNOWLEDGMENTS

The authors acknowledge the Academic Research Fund Tier 1 from Ministry of Education, Singapore (Grant M401050000). A*STAR Computational Resource Centre, Singapore, is acknowledged for providing computational support. J.A.B. acknowledges financial support from the Russian Science Foundation grant 14-13-00982. S.V.D. thanks the Russian Government Program 5-100-2020 for financial support.

REFERENCES

(1) Novoselov, K. S.; Geim, A. K.; Morozov, S. V.; Jiang, D.; Zhang, Y.; Dubonos, S. V.; Grigorieva, I. V.; Firsov, A. A. Electric Field Effect in Atomically Thin Carbon Films. *Science* **2004**, *306*, 666−669.

(2) Baimova, J. A.; Dmitriev, S. V.; Zhou, K.; Savin, A. V. Unidirectional ripples in strained graphene nanoribbons with clamped edges at zero and finite temperatures. *Phys. Rev. B* **2012**, *86*, 035427.

(3) Lee, C.; Wei, X.; Kysar, J. W.; Hone, J. Measurement of the Elastic Properties and Intrinsic Strength of Monolayer Graphene. *Science* **2008**, *321*, 385−388.

(4) Zhang, L.; Zeng, X.; Wang, X. Programmable Hydrogenation of Graphene for Novel Nanocages. *Sci. Rep.* **2013**, *3*, 3162.

(5) Becton, M.; Zhang, L.; Wang, X. Effects of Surface Dopants on Graphene Folding by Molecular Simulations. *Chem. Phys. Lett.* **2013**, *584*, 135−141.

(6) Deng, Z.; Smolyanitsky, A.; Li, Q.; Feng, X.-Q.; Cannara, R. J. Adhesion-dependent Negative Friction Coefficient on Chemically Modified Graphite at the nanoscale. *Nat. Mater.* **2012**, *12*, 1032−1037.

(7) Seol, J. H.; Jo, I.; Moore, A. L.; Lindsay, L.; Aitken, Z. H.; Pettes, M. T.; Li, X.; Yao, Z.; Huang, R.; Broido, D.; Mingo, N.; Ruoff, R. S.; Shi, L. Two-Dimensional Phonon Transport in Supported Graphene. *Science* **2010**, *328*, 213−216.

(8) Liu, B.; Reddy, C. D.; Jiang, J.; Baimova, J. A.; Dmitriev, S. V.; Nazarov, A. A.; Zhou, K. Morphology and In-Plane Thermal Conductivity of Hybrid Graphene Sheets. *Appl. Phys. Lett.* **2012**, *101*, 211909.

(9) Baimova, J. A.; Dmitriev, S. V.; Zhou, K. Discrete breather clusters in strained graphene. *Europhys. Lett.* **2012**, *100*, 36005.

(10) Liu, B.; Baimova, J. A.; Dmitriev, S. V.; Wang, X.; Zhu, H.; Zhou, K. Discrete breathers in hydrogenated graphene. *J. Phys. D: Appl. Phys.* **2013**, *46*, 305302.

(11) Vogt, P.; Padova, P. De; Quaresima, C.; Avila, J.; Frantzeskakis, E.; Asensio, M. C.; Resta, A.; Ealet, B.; Le Lay, G. Silicene: Compelling Experimental Evidence for Graphene-Like Two-Dimensional Silicon. *Phys. Rev. Lett.* **2012**, *108*, 155501.

(12) Lalmi, B.; Oughaddou, H.; Enriquez, H.; Kara, A.; Vizzini, S.; Ealet, B.; Aufray, B. Epitaxial Growth of a Silicene Sheet. *Appl. Phys. Lett.* **2010**, *97*, 223109.

(13) Cahangirov, S.; Topsakal, M.; Akturk, E.; Sahin, H.; Ciraci, S. Two- and One-Dimensional Honeycomb Structures of Silicon and Germanium. *Phys. Rev. Lett.* **2009**, *102*, 236804.

(14) Liu, C. C.; Feng, W.; Yao, Y. Quantum Spin Hall Effect in Silicene and Two-Dimensional Germanium. *Phys. Rev. Lett.* **2011**, *107*, 076802.

(15) Drummond, N. D.; Zolyomi, V.; Fal'ko, V. I. Electrically Tunable Band Gap in Silicene. *Phys. Rev. B* **2012**, *85*, 075423.

(16) Geim, A. K.; Grigorieva, I. V. Van der Waals Heterostructures. *Nature* **2013**, *499*, 419−425.

(17) Haigh, S. J.; Gholinia, A.; Jalil, R.; Romani, S.; Britnell, L.; Elias, D. C.; Novoselov, K. S.; Ponomarenko, L. A.; Geim, A. K.; Gorbachev, R. Cross-Sectional Imaging of Individual Layers and Buried Interfaces of Graphene-Based Heterostructures and Superlattices. *Nat. Mater.* **2012**, *11*, 764−767.

(18) Britnell, L.; Gorbachev, R. V.; Jalil, R.; Belle, B. D.; Schedin, F.; Mishchenko, A.; Georgiou, T.; Katsnelson, M. I.; Eaves, L.; Morozov, S. V.; Peres, N. M. R.; Leist, J.; Geim, A. K.; Novoselov, K. S.; Ponomarenko, L. A. Field-Effect Tunneling Transistor Based on Vertical Graphene Heterostructures. *Science* **2012**, *335*, 947−950.

(19) Georgiou, T.; Jalil, R.; Belle, B. D.; Britnell, L.; Gorbachev, R. V.; Morozov, S. V.; Gholinia, A.; Haigh, S. J.; Makarovsky, O.; Eaves, L.; Ponomarenko, L. A.; Geim, A. K.; Novoselov, K. S.; Mishchenko, A. Vertical Field-Effect Transistor Based on Graphene-WS_2 Heterostructures for Flexible and Transparent Electronics. *Nat. Nanotechnol.* **2013**, *8*, 100−103.

(20) Yu, S.; Li, X. D.; Wu, S. Q.; Wen, Y. H.; Zhou, S.; Zhu, Z. Z. Novel Electronic Structures of Superlattice Composed of Graphene and Silicene. *Mater. Res. Bull.* **2014**, *50*, 268−272.

(21) Zhou, R.; Voon, L. C. L. Y.; Zhuang, Y. Properties of Two-Dimensional Silicon Grown on Graphene Substrate. *J. Appl. Phys.* **2013**, *114*, 093711.

(22) Neek-Amal, M.; Sadeghi, A.; Berdiyorov, G. R.; Peeters, F. M. Realization of Free-Standing Silicene Using Bilayer Graphene. *Appl. Phys. Lett.* **2013**, *103*, 261904.

(23) Cai, Y.; Chuu, C. P.; Wei, C. M.; Chou, M. Y. Stability and Electronic Properties of Two-Dimensional Silicene and Germanene on Graphene. *Phys. Rev. B* **2013**, *88*, 245408.

(24) Hu, W.; Li, Z.; Yang, J. Structural, Electronic, and Optical Properties of Hybrid Silicene and Graphene Nanocomposite. *J. Chem. Phys.* **2013**, *139*, 154704.

(25) Freitag, M.; Steiner, M.; Martin, Y.; Perebeinos, V.; Chen, Z.; Tsang, J. C.; Avouris, P. Energy Dissipation in Graphene Field-Effect Transistors. *Nano Lett.* **2009**, *9*, 1883−1888.

(26) Hu, M.; Zhang, Xi.; Poulikakos, D. Anomalous Thermal Response of Silicene to Uniaxial Stretching. *Phys. Rev. B* **2014**, *87*, 195417.

(27) Jing, Y.; Hu, M.; Guo, L. Thermal Conductivity of Hybrid Graphene/Silicon Heterostructures. *J. Appl. Phys.* **2013**, *114*, 153518.

(28) Zhang, X.; Xie, H.; Hu, M.; Bao, H.; Yue, S.; Qin, G.; Su, G. Thermal Conductivity of Silicene Calculated Using an Optimized Stillinger-Weber Potential. *Phys. Rev. B* **2014**, *89*, 054310.

(29) Xie, H.; Hu, M.; Bao, H. Thermal Conductivity of Silicene from First-Principles. *Appl. Phys. Lett.* **2014**, *104*, 131906.

(30) Liu, B.; Reddy, C. D.; Jiang, J.; Zhu, H.; Baimova, J. A.; Dmitriev, S. V.; Zhou, K. Thermal Conductivity of Silicene Nanosheets and the Effect of Isotopic Doping. *J. Phys. D: Appl. Phys.* **2014**, *47*, 165301.

(31) Xu, Z.; Buehler, M. J. Heat Dissipation at a Graphene-Substrate Interface. *J. Phys.: Condens. Matter* **2012**, *24*, 475305.

(32) Mak, K. F.; Lui, C. H.; Heinz, T. F. Measurement of the Thermal Conductance of the Graphene/SiO_2 Interface. *Appl. Phys. Lett.* **2010**, *97*, 221904.

(33) Ong, Z.-Y.; Pop, E. Molecular Dynamics Simulation of Thermal Boundary Conductance between Carbon Nanotubes and SiO_2. *Phys. Rev. B* **2010**, *81*, 155408.

(34) Moniruzzaman, M.; Winey, K. I. Polymer Nanocomposites Containing Carbon Nanotubes. *Macromolecules* **2006**, *39*, 5194−5205.

(35) Shenogin, S.; Bodapati, A.; Xue, L.; Ozisik, R.; Keblinski, P. Effect of Chemical Functionalization on Thermal Transport of Carbon Nanotube Composites. *Appl. Phys. Lett.* **2004**, *85*, 2229−2231.

(36) Konatham, D.; Striolo, A. Thermal Boundary Resistance at the Graphene-Oil Interface. *Appl. Phys. Lett.* **2009**, *95*, 163105.

(37) Wang, H.; Gong, J.; Pei, Y.; Xu, Z. Thermal Transfer in Graphene-Interfaced Materials: Contact Resistance and Interface Engineering. *ACS Appl. Mater. Interfaces* **2013**, *5*, 2599−2603.

(38) Elias, D. C.; Nair, R. R.; Mohiuddin, T. M. G.; Morozov, S. V.; Blake, P.; Halsall, M. P.; Ferrari, A. C.; Boukhvalov, D. W.; Katsnelson, M. I.; Geim, A. K.; Novoselov, K. S. Control of Graphene's Properties by Reversible Hydrogenation: Evidence for Graphane. *Science* **2009**, *323*, 610−613.

(39) Reddy, C. D.; Zhang, Y. W.; Shenoy, V. B. Patterned Graphone-A Novel Template for Molecular Packing. *Nanotechnology* **2012**, *23*, 165303.
(40) Reddy, C. D.; Zhang, Y. W. Structure Manipulation of Graphene by Hydrogenation. *Carbon* **2014**, *69*, 86−91.
(41) Balog, R.; Jorgensen, B.; Nilsson, L.; Andersen, M.; Rienks, E.; Bianchi, M.; Fanetti, M.; Laegsgaard, E.; Baraldi, A.; Lizzit, S.; Sljivancanin, Z.; Besenbacher, F.; Hammer, B.; Pedersen, T. G.; Hofmann, P.; Hornekaer, L. Bandgap Opening in Graphene Induced by Patterned Hydrogen Adsorption. *Nat. Mater.* **2010**, *9*, 315−319.
(42) Ma, Y.; Dai, Y.; Guo, M.; Niu, C.; Huang, B. Graphene Adhesion on MoS_2 Monolayer: An ab initio study. *Nanoscale* **2011**, *3*, 3883−3887.
(43) Plimpton, S. Fast Parallel Algorithms for Short-Range Molecular-Dynamics. *J. Comput. Phys.* **1995**, *117*, 1−19.
(44) Brenner, D. W.; Shenderova, O. A.; Harrison, J. A.; Stuart, S. J.; Ni, B.; Sinnott, S. B. A Second-Generation Reactive Empirical Bond Order (REBO) Potential Energy Expression for Hydrocarbons. *J. Phys.: Condens. Matter* **2002**, *14*, 783−802.
(45) Stillinger, F. H.; Weber, T. A. Computer-Simulation of Local Order in Condensed Phases of Silicon. *Phys. Rev. B* **1985**, *31*, 5262−5271.
(46) Liu, B.; Baimova, J. A.; Reddy, C. D.; Dmitriev, S. V.; Law, W. K.; Feng, X. Q. Interface Thermal Conductance and Rectification in Hybrid Graphene/Silicene Monolayer. *Carbon* **2014**, *79*, 236−244.
(47) Rappe, A. K.; Casewit, C. J.; Colwell, K. S.; Goddard, W. A.; Skiff, W. M.; UFF, A. Full Periodic-Table Force-Field for Molecular Mechanics and Molecular-Dynamics Simulations. *J. Am. Chem. Soc.* **1992**, *114*, 10024−10035.
(48) Carlborg, C. F.; Shiomi, J.; Maruyama, S. Thermal Boundary Resistance between Single-Walled Carbon Nanotubes and Surrounding Matrices. *Phys. Rev. B* **2008**, *78*, 205406.
(49) Hu, L.; Desai, T.; Keblinski, P. Determination of Interfacial Thermal Resistance at the Nanoscale. *Phys. Rev. B* **2011**, *83*, 195423.
(50) Zhang, J.; Wang, Y.; Wang, X. Rough Contact is Not Always Bad for Interfacial Energy Coupling. *Nanoscale* **2013**, *5*, 11598−11603.
(51) Chen, L.; Huang, Z.; Kumar, S. Phonon Transmission and Thermal Conductance across Graphene/Cu Interface. *Appl. Phys. Lett.* **2013**, *103*, 123110.
(52) Luo, T.; Lloyd, J. R. Enhancement of Thermal Energy Transport across Graphene/Graphite and Polymer Interfaces: A Molecular Dynamics Study. *Adv. Funct. Mater.* **2012**, *22*, 2495−502.
(53) Zhang, H. J.; Lee, G.; Cho, K. Thermal Transport in Graphene and Effects of Vacancy Defects. *Phys. Rev. B* **2011**, *84*, 115460.
(54) Hu, J. N.; Ruan, X. L.; Chen, Y. P. Thermal Conductivity and Thermal Rectification in Graphene Nanoribbons: A Molecular Dynamics Study. *Nano Lett.* **2009**, *9*, 2730−5.
(55) Hu, M.; Keblinski, P.; Li, B. Thermal Rectification at Silicon-Amorphous Polyethylene Interface. *Appl. Phys. Lett.* **2008**, *92*, 211908.
(56) Pei, Q. X.; Zhang, Y. W.; Sha, Z. D.; Shenoy, V. B. Carbon Isotope Doping Induced Interfacial Thermal Resistance and Thermal Rectification in Graphene. *Appl. Phys. Lett.* **2012**, *100*, 101901.
(57) Pei, Q. X.; Sha, Z. D.; Zhang, Y. W. A Theoretical Analysis of the Thermal Conductivity of Hydrogenated Graphene. *Carbon* **2011**, *49*, 4752−4759.
(58) Zhou, J.; Wang, Q.; Sun, Q.; Chen, X. S.; Kawazoe, Y.; Jena, P. Ferromagnetism in Semihydrogenated Graphene Sheet. *Nano Lett.* **2009**, *9*, 3867−3870.

■ NOTE ADDED AFTER ASAP PUBLICATION

This article published ASAP on October 13, 2014. The name of the fourth author has been revised. The corrected version was published ASAP on October 13, 2014.